



Beaming Effect in TeV Blazars

Yanjun Qian¹, Shuochun Wang¹, Peizhen Hu¹, Hengji Zhang¹, Caijun Li¹, Chengye Liu¹, Xiuying Zhao¹, Jianhong Cao¹, Zhiyuan Pei^{1,2,3,4} , and Junhui Fan^{1,2,3,4}

¹ School of Physics and Materials Science, Guangzhou University, Guangzhou 510006, People's Republic of China; peizy@gzhu.edu.cn

² Center for Astrophysics, Guangzhou University, Guangzhou 510006, People's Republic of China

³ Astronomy Science and Technology Research Laboratory of Department of Education of Guangdong Province, Guangzhou 510006, People's Republic of China

⁴ Key Laboratory for Astronomical Observation and Technology of Guangzhou, Guangzhou 510006, People's Republic of China

Received 2025 August 5; revised 2025 November 3; accepted 2025 November 13; published 2025 December 1

Abstract

The detection of TeV emission in extragalactic galaxies has prompted investigations into the beaming effect in blazars, a key feature of relativistic jets modulating multiwavelength radiation, yet quantitative constraints remain limited. This study aims to systematically analyze the beaming effect in TeV blazars by disentangling the beamed and unbeamed components of high-energy spectra and estimating Doppler factors across X-ray, γ -ray, and TeV bands. We also probe the de-beamed (intrinsic) luminosities in these high-energy bands. A comprehensive sample of 51 TeV blazars is compiled. A two-component model is applied to decompose core-dominated and extended emissions, and Doppler factors are derived from the core-dominance parameters and the jet geometries. Low-synchrotron-peaked sources exhibit the strongest beaming, confirming that high-energy core-dominance parameters serve as robust tracers of the beaming effect. Doppler factors are highest in the γ -ray band and show a concave-to-convex evolution from radio to TeV bands, suggesting distinct emission regions or viewing angles. Derived Doppler factors enable the calculation of de-beamed intrinsic luminosities, offering insights into the blazar jet's intrinsic properties.

Supplementary material for this article is available [online](#)

Unified Astronomy Thesaurus concepts: [Blazars \(164\)](#); [Gamma-ray sources \(633\)](#); [Jets \(870\)](#)

1. Introduction

Blazars are radio-loud active galactic nucleus (AGNs) with relativistic jets that are powered by accretion onto a central supermassive black hole and closely aligned with our line of sight (Begelman et al. 1984; Urry & Padovani 1995; Blandford et al. 2019). Due to the relativistic beaming, their emission is dominated by the jet non-thermal component, making them variable broadband emitters from radio to γ -ray energies (Marscher 2016). Blazars show many prominent observational properties, such as high polarization, fast rapid variability, superluminal motion of jet components, dominance of non-thermal continuum in the core, and strong high-energy γ -ray radiation, etc. (Wills et al. 1992; Romero et al. 2002; Fan et al. 2013; Pei et al. 2016, 2020a, 2023; Xiao et al. 2022; Yang et al. 2023, and references therein). Blazars are categorized into BL Lac objects (BL Lacs) and flat spectrum radio quasars (FSRQs) based on the rest-frame equivalent width (EW) of their broad optical emission lines, with BL Lac sources having $EW < 5 \text{ \AA}$ and those with $EW \geq 5 \text{ \AA}$ classified as FSRQs (Stickel et al. 1991).

The spectral energy distribution of blazars spans from radio frequencies to high-energy γ -rays, characterized by two broad humps. The low-energy peak occurring at infrared to UV/X-ray energy regime is believed to be produced by the synchrotron process, whereas the high-energy hump from inverse Compton mechanism peaks in the MeV/GeV range is attributed to the inverse Compton scattering (Tavecchio et al. 1998; Ghisellini & Tavecchio 2009; Böttcher 2019; Cerutti 2020; Tan et al. 2020). The maximum of the second peak shifts from the most powerful FSRQs in the MeV band, to the TeV band for BL Lacs.

Based on the location of the synchrotron peak frequency (ν_p), BL Lacs (and also FSRQs) can be classified as low-energy peaked sources (LBLs, $\log(\nu_p/\text{Hz}) < 14.0$), intermediate-energy peaked sources (IBLs, $14.0 < \log(\nu_p/\text{Hz}) < 15.0$), and high-energy peaked sources (HBLs, $15.0 < \log(\nu_p/\text{Hz}) < 17.0$) (Abdo et al. 2010a; Fan et al. 2016; Yang et al. 2022a). In the most peculiar case, the synchrotron peak can occur at even higher frequencies by up to two orders of magnitude for the so-called extreme HBLs (EHBLs, $\log(\nu_p/\text{Hz}) > 17.0$, Costamante et al. 2001; Biteau et al. 2020). EHBLs are considered as the most

efficient and extreme particle accelerators in Universe, having their TeV peak at energies >1 TeV with a hard intrinsic TeV spectrum. Beaming effect plays an important role in the blazar-jet environment that the emission of jets is predominantly influenced by relativistic beaming effect. When a sub-source moves at relativistic velocity, the corresponding Doppler factor, also known as the beaming factor, can be calculated via $\delta = [\Gamma(1 - \beta \cos \theta)]^{-1}$, where $\Gamma = (1 - \beta^2)^{-\frac{1}{2}}$ ($\beta = \frac{v}{c}$) denotes the Lorentz factor of the jet, θ is the angle between the jet and the observer's line of sight (Ghisellini et al. 1993; Urry & Padovani 1995; Fan et al. 2011; Pei et al. 2016). Among all AGNs, blazars exhibit the smallest radial angle (typically $<5^\circ$), thus resulting in a large Doppler factor and the strongest beaming effect (Hovatta et al. 2009; Pei et al. 2020a, 2020b; Yang et al. 2022b; Zeng et al. 2022). Therefore, investigating the beaming effect can provide valuable insights into the nature of blazars and contribute to our understanding of the evolution of AGN.

However, the beaming Doppler factor cannot be calculated precisely since it is not an observable quantity, and there are difficulties in estimating δ in high energy band, e.g., from X-ray to TeV emission, due to undetectable viewing angle within blazar jets in high energy band. In this work, we will propose a new method to estimate the Doppler factors in high energy emission.

The very high energies (VHE, $\gtrsim 100$ GeV) from blazars are normally detected by the ground-based Imaging Air Cherenkov Telescopes (IACTs). To date, 84 TeV blazars are captured with the majority of them being HBLs (including 16 EHBLs), which are listed in TeVCat 2.0.⁵ Mrk 421, probably the brightest and the most studied object by astronomers, was the first detection of TeV emission (Punch et al. 1992), and it was found that the characteristic of the flux variability in both the GeV and TeV bands seems to be similar, with the TeV flaring states being coincident with that observed in the GeV band. This behavior is found in many TeV blazars gradually, indicating the GeV/TeV emission appears closely connective. Lin & Fan (2016) compared the multi-wavelength flux densities from radio to γ -ray and photon indices in X-ray and γ -ray bands for 47 TeV-detected BL Lacs (TBLs) and 615 non-TeV-detected BL Lacs (non-TBLs), and concludes that the former behaves significantly different from the latter. Similarly, Liang et al. (2023) found the mid-IR luminosity of the TBLs is on average higher than that of non-TBLs, whereas the average mid-IR spectral index of TBLs is smaller than the non-TBLs, suggesting that the TBLs are brighter and hold a more flat spectrum than do the non-TBLs in the mid-IR band. Paiano et al. (2021) analyzed 55 Fermi-detected BL Lacs with hard γ -ray spectrum, and predicted the detectability for the expected VHE by IACTs.

⁵ <https://tevcat2.tevcat.org/>

Over the past 20 yr, TeV astronomy has evolved from a nascent field with only a few sources to a fully developed discipline, expanding our knowledge of various types of TeV gamma-ray sources. These observations have provided a deeper insight into numerous important questions in high-energy astrophysics and astroparticle physics (Bose et al. 2022; Sitarek 2022). Since blazars occupy the majority of TeV AGNs, thus we believe the beaming effect in TeV blazars is worth researching that paving us a new way to explore the VHE mechanism. We also put forward a novel method to estimate the Doppler factors in X-ray, γ -ray, and TeV band respectively for TeV-detected blazars. This paper is organized as follows: in Section 2 we present the method of our analysis and describe the source sample in Section 3. Result and discussion will be stated in Section 4 and the conclude findings within this work in Section 5. Throughout this paper, we take the Λ -CDM model with $\Omega_\Lambda \simeq 0.73$, $\Omega_M \simeq 0.27$, and $H_0 \simeq 68 \text{ km s}^{-1} \text{ Mpc}^{-1}$ (Planck Collaboration et al. 2014).

2. Method

2.1. Radio Core-dominance Parameter

The observed radio emission in blazars can be decomposed into beamed (core) and unbeamed (extended) components: $L_{\text{obs}} = L_{\text{core}} + L_{\text{ext}}$. The ratio $R_{\text{radio}} = L_{\text{core}}/L_{\text{ext}}$ defines the radio core-dominance parameter, which serves as a key beaming indicator (Orr & Browne 1982; Urry & Shafer 1984; Fan et al. 2011; Pei et al. 2019, 2020d). Within the relativistic beaming model, R_{radio} relates to the kinematic parameters (δ , Γ , β , θ) as (e.g., Ghisellini et al. 1993; Urry & Padovani 1995; Fan 2003; Pei et al. 2016, 2020b):

$$R_{\text{radio}} = f \Gamma^{-p} [(1 - \beta \cos \theta)^{-p} + (1 + \beta \cos \theta)^{-p}], \quad (1)$$

where $f = S_{\text{core}}^{\text{int}}/S_{\text{ext}}^{\text{int}}$ is the intrinsic core-to-extended flux ratio in the comoving frame, and $p = 2 + \alpha$ for a continuous jet or $p = 3 + \alpha$ for a discrete blob (α is the spectral index). For small viewing angles ($\theta \lesssim 5^\circ$), this simplifies to:

$$R_{\text{radio}} \simeq f \delta^p, \quad (2)$$

where $\delta = [\Gamma(1 - \beta \cos \theta)]^{-1}$ is the Doppler factor. Thus, R_{radio} provides a direct probe of the beaming strength. The value of R_{radio} at transverse alignment ($\theta = 90^\circ$) is denoted $R_{\perp\text{radio}}$. For a continuous jet ($p = 2 + \alpha$), Orr & Browne (1982) derived $R_{\perp\text{radio}} = 2f/\Gamma^p$, leading to:

$$R_{\text{radio}} = R_{\perp\text{radio}} \cdot \frac{1}{2} [(1 - \beta \cos \theta)^{-p} + (1 + \beta \cos \theta)^{-p}]. \quad (3)$$

Based on a sample of 32 FSRQs, Orr & Browne (1982) estimated $R_{\perp\text{radio}} \approx 0.024$ at 5 GHz. Recently, Pei et al. (2023) obtained a median value of $R_{\perp\text{radio}} = 0.032$ from 226 blazars, suggesting that $\sim 97\%$ of the total radio emission arises from the beamed component. In this work, we adopt the radio core-dominance parameters from Pei et al. (2016, 2019, 2020a),

who compiled the largest catalog to date with R_{radio} measurements for 4388 AGNs, including over 1300 blazars.

2.2. Core-dominance Parameter in High-energy Bands

It is quite interesting to note that the nearest TeV-detected radio galaxy, Centaurus A ($z = 0.00183$, also known as NGC 5128), has been shown the central core and extended giant lobe clearly in the radio and γ -ray band (Abdo et al. 2010b; Feain et al. 2011). The core is only 10 lt-day across while the lobe is up to kilo-parsec scale, and the jet is observed in both radio and X-ray images. Centaurus A is identified as a Fanaroff-Riley type I (FRI) radio galaxy. Since FRI galaxies are believed to be the parent population of BL Lacs (Urry & Padovani 1995; Fan et al. 2011; Ye et al. 2023), we consider the total luminosity from X-ray to TeV in blazars can also be resolved into two components, and the core-dominance parameters are effective beaming indicators. We extend the two-component beaming model to high-energy bands (X-ray, γ -ray, TeV), where the core component cannot be directly resolved. The key assumption is that the kinematic parameter $\beta \cos \theta$, derived from radio observations, remains unchanged across bands. (e.g., Pei et al. 2020b; Zeng et al. 2022; Zhang et al. 2022) For a continuous jet ($p = 2 + \alpha_i$, α_i is the spectral index in band i , $i = \text{X-ray, } \gamma\text{-ray and TeV}$), the core-dominance parameter in band i is:

$$R_i = \frac{L_{i,\text{core}}}{L_{i,\text{ext}}} = R_{\perp i} \cdot g_i(\beta, \cos \theta), \quad (4)$$

where $R_{\perp i}$ is the transverse ratio and the beaming function is:

$$g_i(\beta, \cos \theta) = \frac{1}{2} \left[(1 - \beta \cos \theta)^{-(2+\alpha_i)} + (1 + \beta \cos \theta)^{-(2+\alpha_i)} \right]. \quad (5)$$

Throughout the paper, we adopt the spectral index in the X-ray, γ -ray and TeV band from Zeng et al. (2022), 4FGL-DR4 catalog (Ballet et al. 2023), and TeV Cat2.0, respectively, for our calculation. The parameter $\beta \cos \theta$ is obtained from Equation (3) using radio data, and $R_{\perp i}$ is determined empirically as described below.

2.3. Determination of $R_{\perp i}$

The transverse ratio $R_{\perp i}$ is determined by minimizing the scatter between the observed high-energy luminosity and the predicted beamed luminosity. We illustrate the procedure for the TeV band following Zhang et al. (2022), who found a tight correlation between TeV and radio core luminosities for 51 TeV blazars: $\log L_{\text{TeV}} = (0.74 \pm 0.09)\log L_{\text{r,b}} + (13.61 \pm 3.54)$. Assuming this correlation holds universally, the beamed TeV luminosity is $L_{\text{TeV,b}} = kL_{\text{r,b}}^{0.74}$. The total TeV

luminosity is then:

$$L_{\text{TeV}} = L_{\text{TeV,b}} \left(1 + \frac{1}{R_{\text{TeV}}} \right) = kL_{\text{r,b}}^{0.74} \left[1 + \frac{1}{R_{\perp \text{TeV}} g_{\text{TeV}}(\beta, \phi)} \right], \quad (6)$$

where $R_{\text{TeV}} = R_{\perp \text{TeV}} g_{\text{TeV}}$. The constants k and $R_{\perp \text{TeV}}$ are determined by minimizing $\Sigma[\log(L_{\text{TeV}}/L_{\text{TeV}}^{\text{obs}})]^2$ over the sample, yielding $R_{\perp \text{TeV}} = 1.60 \times 10^{-4}$ with uncertainty of $\sigma_{R_{\perp \text{TeV}}} = 0.18$ dex. The same method is applied to X-ray and γ -ray bands, giving $R_{\perp \text{X}} = 2.27 \times 10^{-3}$ with uncertainty of $\sigma_{R_{\perp \text{X}}} = 0.15$ dex (Zeng et al. 2022) and $R_{\perp \gamma} = 3.05 \times 10^{-3}$ with $\sigma_{R_{\perp \gamma}} = 0.12$ dex (Pei et al. 2020b). In this work, we adopt these values for the following calculation, and the error propagations for different band are also taken into consideration.

2.4. Spectral Index Decomposition

The observed spectral index α_{total} can be decomposed into beamed and unbeamed components (Fan et al. 2010):

$$\alpha_{\text{total}} = \frac{R}{1+R} \alpha_{\text{beamed}} + \frac{1}{1+R} \alpha_{\text{unbeamed}}, \quad (7)$$

where R is the core-dominance parameter. This has been applied to radio spectra of Fermi blazars, yielding flat beamed components ($\alpha_{\text{beamed}} \approx 0$) and steeper unbeamed components (Pei et al. 2020a). We extend this decomposition to high-energy bands:

$$\alpha_{\text{total}}^i = \frac{R_i}{1+R_i} \alpha_{\text{beamed}}^i + \frac{1}{1+R_i} \alpha_{\text{unbeamed}}^i, \quad (8)$$

where α_{total}^i , α_{beamed}^i , and $\alpha_{\text{unbeamed}}^i$ are the spectral indices in band i .

2.5. Doppler Factor Estimation

In the context of beaming source, Equation (2) can be described the relation between two beaming indicators in the radio band, i.e., radio core-dominance parameter and Doppler factor. Based on the discussion above, the beaming framework lying in high energy band allows us to explore the Doppler factor estimation in the X-ray, γ -ray and TeV emission. In this sense, we can assume the relation between two beaming indicators are also adoptable into the high energy emission and therefore Equation (2) can be extended to

$$R_i = f_i \delta_i^p \quad (i = \text{X, } \gamma \text{ and TeV}), \quad (9)$$

where R_i is the derived core-dominance parameter in i band, f_i is an intrinsic constant in each band, δ_i is the Doppler factor in corresponding energy band, and $p = 2 + \alpha^i$ for continuous jet or $3 + \alpha^i$ for spherical blob, where α^i is the spectral index in each energy band.

For starters, α^{radio} can be taken for 0 since most blazars are flat-spectrum radio AGNs, thus in the radio band, one can

Table 1
Sample of 51 TeV Blazars

TeV Name (1)	Class (2)	z (3)	$\log R_{\text{radio}}$ (4)	$\log R_X$ (5)	$\log R_\gamma$ (6)	$\log R_{\text{TeV}}$ (7)	$\log L_{\text{radio}}$ (8)	$\log L_X^{\text{in}}$ (9)	$\log L_\gamma^{\text{in}}$ (10)	$\log L_{\text{TeV}}^{\text{in}}$ (11)	α_X (12)	α_γ (13)	α_{TeV} (14)	δ (15)	References (16)	δ_X^* (17)	δ_γ^* (18)	δ_{TeV}^* (19)
J0112+227	IBL	0.36	1.93	2.18	5.02	6.03	44.37 ± 1.84	44.76 ± 1.53 41.18 ± 2.03	41.58 ± 2.33 39.70 ± 1.31	39.89 ± 2.57 33.38 ± 1.84	1.87	2.08	3.69	25.12	Z20	$6.48^{+0.57}_{-0.95}$ $6.26^{+0.74}_{-1.19}$	$19.87^{+4.12}_{-4.66}$ $18.13^{+5.67}_{-6.03}$	$9.88^{+3.89}_{-3.66}$ $7.78^{+4.79}_{-3.39}$
...

Note. Column (1) gives the source name listed in TeV Cat2.0; column (2) the classification. Three groups are taken into account (HBL, IBL and LBL+FSRQ) in this work; column (3) redshift; columns (4) to (7) list the core-dominance parameters collected from our previous work, covering the radio, X-ray, γ -ray and TeV emission (in form of logarithms); column (8) show the radio luminosities; columns (9) to (11) are the de-beamed luminosities in X-ray, γ -ray and TeV emission. The upper and lower values signify the luminosities are de-beaming within the scenario of continuous jet and blob case, respectively. All luminosities are in units of erg s^{-1} (in form of logarithms); columns (12) to (14) display the spectral indices from X-ray to TeV, which adopted from Zeng et al. (2022), 4FGL-DR4 catalog, and TeV Cat2.0; column (15) gives the radio Doppler factors collected from literature where listed in column (16); columns (17) to (19) are the Doppler factors in high energy bands we derived in this work (marked with asterisks), including X-ray, γ -ray, and TeV band, respectively. Similarly, the upper values give the case for continuous jet and the lower ones are for spherical jet. The upper error and lower error are also given using the MCMC method. Table 1 is published in its entirety in the machine-readable format. Only 1 sources are shown here for guidance regarding its form and content. (The table is available in its entirety in machine-readable form.)

obtain $f_{\text{radio}} = R_{\text{radio}}/\delta_{\text{radio}}^p$ ($p = 2$ or 3). The radio Doppler factor is a well defined quantity and can be estimated by radio observations. We collect δ_{radio} for our sample from the recent literature, and we give preference to the median value if a source have different value of δ_{radio} given by more than one references. We list the collected δ_{radio} in column (15) in Table 1. Combining the radio core-dominance parameter, one can calculate the constant f_{radio} . Previous studies remark that $\Gamma_{\text{radio}}^p = 2f_{\text{radio}}/R_{\perp,\text{radio}}$ (Orr & Browne 1982; Pei et al. 2020b). Recently, we estimate the value of $R_{\perp,\text{radio}} = 0.032$ for a large group with γ -ray blazars (Pei et al. 2023), which allows us to compute the bulk Lorentz factor in the radio emission with regard to both cases $p = 2$ or 3 for each source in our present sample.

In the framework of high energy beaming, the previous relation can yield

$$\Gamma_i^p = \frac{2f_i}{R_{\perp,i}} \quad (10)$$

where Γ_i denotes the bulk Lorentz factor within jet in high energy band. PKS 2155–304 is a HBL (listed in our present sample), which had been reported the TeV flux changed by a factor of 2 in 3–5 minutes (Ghisellini & Tavecchio 2008). This fast variability can be explained by the emitting region is moving with a bulk Lorentz factor $\Gamma_{\text{TeV}} \sim 50$. This source is also found an extremely remarkable flare of γ -ray emission on 2006 July 28, with an average flux more than 10 times the low-state (e.g., Foschini et al. 2008; Tan et al. 2024). A Lorentz factor $\Gamma_\gamma \sim 20$ –50 on γ -ray band can be obtained via using a stochastic dissipation model. H.E.S.S. collaboration reported PKS 2155–304 was found in a low flux state with respect to previous observations but exhibited highly significant flux variability in the X-rays during observation from 2013 June to 2013 October (Abdalla et al. 2020). Adopting a one-zone synchrotron self-Compton (SSC) model, the X-ray emission Lorentz factor $\Gamma_X \sim 10$ –20 was found within jet. Considering this source’s radio Lorentz factor is $\Gamma_{\text{radio}} = 11.45/8.62$ for continuous jet and spherical jet, respectively, we can obtain a relation that $\Gamma_{\text{TeV}} \simeq (1\text{--}2)\Gamma_\gamma \simeq (2\text{--}4)\Gamma_X \simeq (4\text{--}5)\Gamma_{\text{radio}}$.

Another typical source is Mrk 421, the plentiful broadband flux studies has pointed out that $\Gamma_{\text{TeV}} \sim 100$ (e.g., Maraschi et al. 1999; Konopelko et al. 2003), $\Gamma_\gamma \sim 20$ –50 (Shukla et al. 2012), and $\Gamma_X \sim 10$ –20 (Isobe et al. 2014; Acciari et al. 2020), when the source is on a high state in different band. Combining the very long baseline interferometry and Very Large Array observation on Mrk 421 ($\Gamma_{\text{radio}} \sim 10$), we can also conclude that $\Gamma_{\text{TeV}} \gtrsim \Gamma_\gamma \gtrsim \Gamma_X \gtrsim \Gamma_{\text{radio}}$.

Since the Lorentz factors are crucial parameters for estimating the Doppler factors in each band, but the relation among the Lorentz factors in different bands cannot be fixed precisely. We thus employ a Markov Chain Monte Carlo method (hereafter MCMC) for determining the mutual

relationship of Γ_i . MCMC is a powerful class of statistical algorithms designed to sample from complex probability distributions, especially posterior distributions in Bayesian inference. Its core value lies in enabling quantitative analysis of parameters with uncertainties, which is highly relevant to addressing the limitations of fixed Lorentz factors ratio assumptions in this study. Therefore, Γ_i ratios should be treated as free parameters with prior distributions and integrated into the MCMC model to quantify uncertainty propagation. The specific methods we use are divided into the following main steps:

1. Define the proportional coefficients for Γ_i as $\Gamma_{\text{TeV}} = k_1\Gamma_\gamma$, $\Gamma_\gamma = k_2\Gamma_X$, and $\Gamma_X = k_3\Gamma_{\text{radio}}$. At the very beginning, we assume the value of Γ_i satisfies: $\Gamma_{\text{TeV}} \simeq 2.0\Gamma_\gamma$, $\Gamma_\gamma \simeq 2.0\Gamma_X$, and $\Gamma_X \simeq 1.5\Gamma_{\text{radio}}$ for both continuous jet and spherical case, i.e., $k_1 = 2.0$, $k_2 = 2.0$, $k_3 = 1.5$, and Γ_{radio}^p ($p = 2$ or 3) can be determined for each source in our sample. It is noted that if we assume a unity ratios then $k_1 = k_2 = k_3 = 1$.
2. log-normal distributions (or uniform distributions) are adopted for k_1 , k_2 , and k_3 . The uncertainties need to be considered in calculations and can be set with 1σ , i.e., $\sigma_{k_1} = 0.8$, $\sigma_{k_2} = 0.6$, and $\sigma_{k_3} = 0.4$. The prior ranges are determined based on observed Γ_i values of different sources and different states in the literature, e.g., $k_1 = 1$ –4, $k_2 = 1$ –3, $k_3 = 1$ –2, covering variations from low to high states. The values of R_\perp from X-ray to TeV emission are taken with their uncertainties: $R_{\perp,\text{TeV}} = 1.60 \times 10^{-4}$ ($\sigma_{R_{\perp,\text{TeV}}} = 0.18$ dex), $R_{\perp,\gamma} = 3.05 \times 10^{-3}$ ($\sigma_{R_{\perp,\gamma}} = 0.12$ dex) and $R_{\perp,X} = 2.27 \times 10^{-3}$ ($\sigma_{R_{\perp,X}} = 0.15$ dex)
3. We perform the calculating in two-ways: continuous jet and spherical jet. By adopting the Metropolis–Hastings Sampling, at least 20 walkers and 10,000 sampling steps are set. The first 50% of steps are discarded as the burn-in phase.
4. The likelihood function is constructed using a χ^2 statistic. Finally, we can confirm convergence via the Gelman–Rubin test ($R < 1.01$) and trace plots to ensure the parameter chains adequately cover the posterior distribution.

After MCMC, we obtain the best-fit values for k_1 , k_2 and k_3 . Thus Γ_i can be determined in each band for two scenarios of jet. Then f_i can be obtained using Equation (10), and in this case $p = 2 + \alpha^i$ or $p = 3 + \alpha^i$. Finally, the Doppler factors in each band can be estimated via Equation (9): $\delta_i = (R_i/f_i)^{1/p}$. We emphasize that the derived Doppler factors depend on the assumed scaling relations and the jet model. The uncertainties in these assumptions will be propagated in our analysis. We will make the Python code for the MCMC algorithm available as supplementary material.

2.6. Multiwavelength De-beamed Luminosity

The monochromatic luminosity is given by

$$L = 4\pi d_L^2 \nu f_\nu, \quad (11)$$

where f_ν is the K -corrected flux density at the corresponding frequency ν , and d_L is the luminosity distance at redshift z .

For the γ -ray band, the observed γ -ray luminosity is calculated via (Abdo et al. 2010c; Fan et al. 2016; Abdollahi et al. 2020; Yang et al. 2023)

$$L_\gamma^{\text{obs}} = 4\pi d_L^2 (1+z)^{\alpha_\gamma^{\text{ph}} - 2} F_\gamma, \quad (12)$$

where $(1+z)^{\alpha_\gamma^{\text{ph}} - 2}$ denotes the γ -ray flux K -correction, and $\alpha_\gamma^{\text{ph}}$ is the γ -ray photon index. The integral flux F_γ is obtained by $F_\gamma = \int_{E_L}^{E_U} E dN$, with $E_L = 1 \text{ GeV}$ and $E_U = 100 \text{ GeV}$. We collect γ -ray flux data from the 4FGL-DR4 catalog (Ballet et al. 2023) for our TeV sample, calculating γ -ray luminosities in erg s^{-1} based on the first 14 yr of Fermi-LAT survey data.

For TeV luminosity calculation, we employ

$$L_{E \text{ TeV}} = 4\pi d_L^2 (1+z)^{\alpha_{\text{TeV}}^{\text{ph}} - 2} F_{E \text{ TeV}}, \quad (13)$$

where $\alpha_{\text{TeV}}^{\text{ph}}$ is the photon index in the TeV band after Extragalactic Background Light (EBL) deabsorption. The EBL deabsorption is performed using the model of Domínguez et al. (2011) with updates from Saldana-Lopez et al. (2021), Finke et al. (2022) and Domínguez et al. (2024), applying the absorption correction to the observed TeV spectra. The flux $F_{E \text{ TeV}}$ is converted from Crab units using the complete Crab Nebula spectrum:

$$1 \text{ crab} = 2.83 \times 10^{-11} E^{-2.62} \text{ ph cm}^{-2} \text{ s}^{-1} \text{ TeV}^{-1}, \quad (14)$$

where the spectral index $\alpha_{\text{crab}} = 2.62$ and the normalization corresponds to the flux at 1 TeV (Aharonian et al. 2004).

Based on the beaming model, Dermer (1995) and Fan et al. (2013) established that the γ -ray Doppler factor can probe emission mechanisms in blazars. For continuous jets:

$$L_\gamma^{\text{in}} = L_\gamma^{\text{obs}} / \delta_\gamma^{3+\alpha_\gamma}, \quad (15)$$

and for spherical jets:

$$L_\gamma^{\text{in}} = L_\gamma^{\text{obs}} / \delta_\gamma^{4+\alpha_\gamma}. \quad (16)$$

We extend this approach to multiple bands:

$$\begin{aligned} \text{Continuous jets: } & L_i^{\text{in}} = L_i^{\text{obs}} / \delta_{i,\text{cont}}^{3+\alpha_i} \\ \text{Spherical jets: } & L_i^{\text{in}} = L_i^{\text{obs}} / \delta_{i,\text{sph}}^{4+\alpha_i}. \end{aligned} \quad (17)$$

We collect observed TeV luminosities from Zhang et al. (2022) (calculated at $E = 1 \text{ TeV}$), while X-ray and radio luminosities are from Zeng et al. (2022) and Pei et al. (2020a). The de-beamed luminosities with propagated uncertainties are listed in Table 1, with upper values for continuous jets and lower values for spherical blobs. All luminosities are logarithmic and in erg s^{-1} .

3. Sample

Aiming to discover the beaming pattern within the TeV blazars and further explore the TeV emission mechanism, we utilize the sample given by Zhang et al. (2022), which contains 51 sources with available core-dominance parameters in TeV, γ -ray, X-ray and radio band, where R_{TeV} , R_γ , R_X , and R_{radio} are collected from Zhang et al. (2022), Zeng et al. (2022), Pei et al. (2020b) and Pei et al. (2020a), respectively. This sample consisted of 5 FSRQs and 46 BL Lacs (31 HBLs, 13 IBLs and 2 LBLs). Since FSRQs and LBLs are considered to be coming from the same population, we thus group them into a same category. We also estimate the Doppler factors in high energy bands via a robust approach described above. All data are listed in Table 1. Column (1) lists the source name in TeV Cat2.0; column (2) shows their class, which three types are taken into account (HBL, IBL and LBL+FSRQ); column (3) is the redshift; columns (4) to (7) list the core-dominance parameters collected from our previous work, covering the radio, X-ray, γ -ray and TeV emission (in form of logarithms); column (8) show the radio luminosities; columns (9) to (11) are the de-beamed luminosities. All luminosities are in units of erg s^{-1} (in form of logarithms); columns (12) to (14) display the spectral indices from X-ray to TeV, which adopted from Zeng et al. (2022), 4FGL-DR4 catalog, and TeV Cat2.0; column (15) gives the radio Doppler factors collected from literature where listed in column (16); columns (17) to (19) are the Doppler factors in high energy bands we derived in this work (marked with asterisks), including X-ray, γ -ray, and TeV band, respectively. For columns (9) to (11) and (17) to (19), the upper values give the case for continuous jet and the lower ones are for spherical jet.

Our sample compilation from TeV-detected sources introduces selection effects that may couple luminosity, beaming, and redshift in non-trivial ways. TeV photons suffer from absorption by the EBL that increases with redshift, making high- z detections biased toward sources with higher intrinsic luminosities or stronger beaming. This selection effect is partially mitigated by our EBL deabsorption procedure, but residual biases may affect the derived relationships. We note that our results should be interpreted in the context of this TeV-selected sample. For further comparison, TeVCat 2.0 lists 85 blazars, of which 70 have available redshift measurements, with a mean value of 0.196 ± 0.127 . Our present sample comprises 51 TeV blazars, with a mean redshift of 0.192 ± 0.116 , which is consistent with the full TeV sample. The multiwavelength luminosities will also be affected by the beaming effect, thus, deriving de-beamed luminosities is crucial. We present our results in the following sections.

4. Result and Discussion

4.1. Multiwavelength Core-dominance Parameters

The distributions of the multiwavelength core-dominance parameters for TeV blazars is shown in Figure 1. We classify

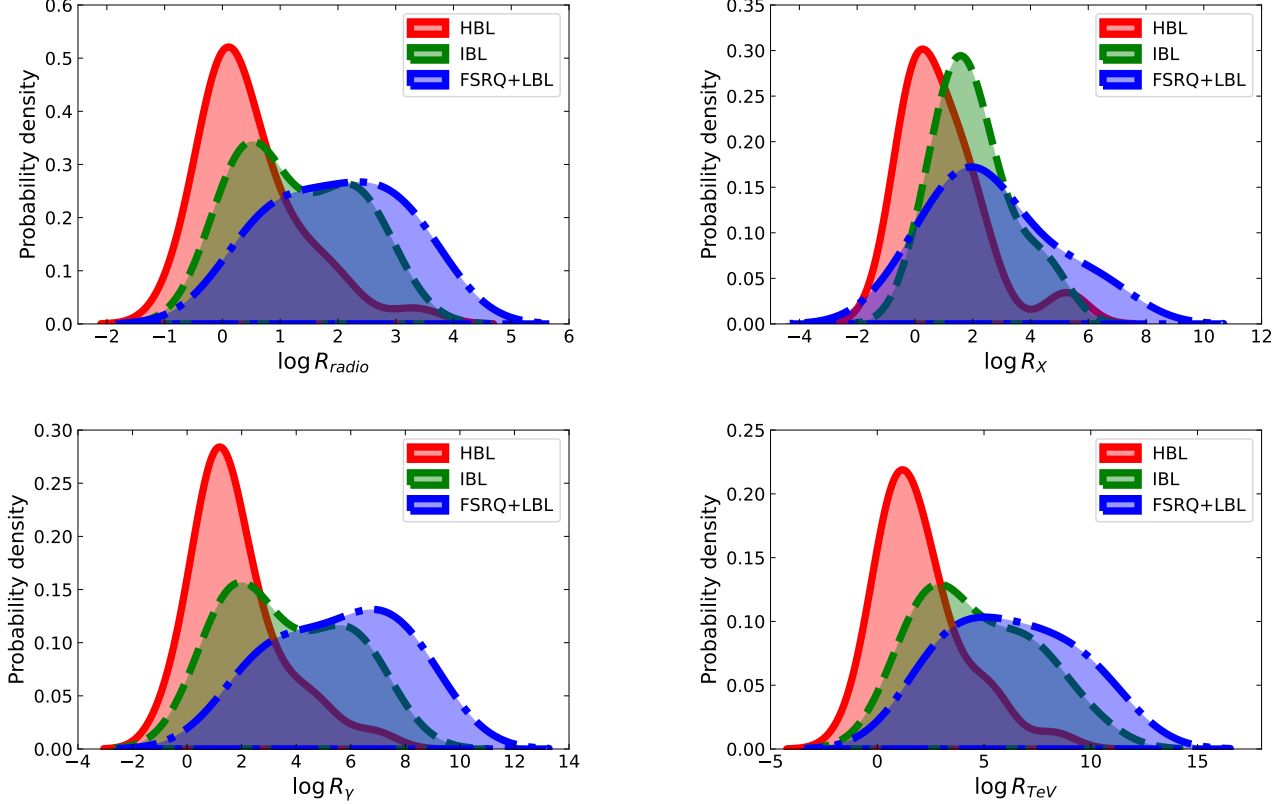


Figure 1. Distributions of core-dominance parameters for radio, X-ray, γ -ray and TeV emission. The red-shaded region refers to high synchrotron peak, or high-energy BL Lacs (HBLs), the green one denotes the intermediate BL Lacs (IBLs), and the blue one signifies the group combined with low BL Lacs (LBLs) and FSRQs. All the values of core-dominance parameters are in logarithm.

our sample into three groups, HBL/IBL/FSRQ+LBL, which are labeled in the red-shaded areas, green-shaded areas and blue-shaded areas, respectively. A clear tendency that a downward trend in the peak value as the core-dominance parameter increases is first catching our eye. This trend can be interpreted as a decrease in the viewing angle, indicating an enhanced beaming effect and an increased Doppler factor.

The first distribution refers to the radio core-dominance parameters, $\log R_{\text{radio}}$. The average value for 31 HBLs is $\langle \log R_{\text{radio}} \rangle = 0.50 \pm 0.89$ with a median of 0.16. The peak of probability density is beyond half ($\rho = 0.52$), situating at $\log R_{\text{radio}} = 0.11$. On the other hand, the peak for 13 IBLs is placed in $\log R_{\text{radio}} = 0.53$ with a distribution density $\rho = 0.34$, and also has an obtuse peak located in $\log R_{\text{radio}} = 2.13$ with $\rho = 0.26$. The average value for IBLs sample is $\langle \log R_{\text{radio}} \rangle = 1.28 \pm 0.98$ and hold a median of 0.97. Lastly, for 7 FSRQs+LBLs sample, on average we obtain $\langle \log R_{\text{radio}} \rangle = 1.96 \pm 1.12$. The median is 2.16, which is rather close to the average value, making the distribution is quite placid. The distribution peak situates in $\log R_{\text{radio}} = 2.38$ with a density $\rho = 0.27$. The density peak appears that the low-energy synchrotron peak TeV sources are lying broadly in the range of larger radio core-dominance parameters, while the

high-energy synchrotron peak TeV sources are holding the less radio core-dominance parameters. This implies that TeV FSRQs or TeV IBLs have a stronger beaming effect than that of TeV HBLs and TeV IBLs in the radio band, or the viewing angles within former are on average smaller than latter. Based on a large sample with 252 Fermi-detected BL Lacs and 283 Fermi-detected FSRQs with derived radio core-dominance parameters, Pei et al. (2020a) pointed out that there is no significant difference between the γ -loud BL Lacs and γ -loud FSRQs. Our findings here are slightly contradictory to the given result in Pei et al. (2020a) that TeV BL Lacs have smaller $\log R_{\text{radio}}$ with respect to FSRQs, perhaps showing different radio beaming pattern in TeV sources.

Kembhavi (1993) found a tight correlation between the radio core-luminosity and the X-ray total-observed luminosity in blazars, leading us a key to separate the X-ray emission into beamed and unbeamed component in γ -ray loud and TeV-detected blazars. The derived X-ray core-dominance parameters distributions are shown in the second panel in Figure 1. Notably, HBLs and IBLs both possess a sharp peak with comparable probability density at nearby $\rho \simeq 0.30$ in where $\log R_x = 0.27$ and $\log R_x = 1.58$, respectively. Meanwhile, HBLs also peaks in $\log R_x = 5.24$ with density $\rho = 0.03$.

The average value and median of HBLs, $\langle \log R_x \rangle = 0.98 \pm 1.47$ and 0.65 , are obtained. The IBLs subclass in this case exhibit a more concentrated distribution compared with the radio emission behavior, with $\log R_x$ value ranging from 0.10 to 4.80 and an average value of $\langle \log R_x \rangle = 2.03 \pm 1.32$ with a median of 1.76 . For FSRQs+LBLs, $\log R_x$ spans from -0.02 to 6.37 , with an average value of $\langle \log R_x \rangle = 2.66 \pm 2.12$. Similar to $\log R_{\text{radio}}$, this subgroup show a wide region and overlap the other two subsamples. Interestingly, at a distribution density of $\rho = 0.17$, FSRQ+LBLs peaks in $\log R_x = 1.96$, verging on the peak of IBLs. Above results give us a hint that BL Lacs and FSRQs may perform similar beaming pattern in the X-ray band since $\langle \log R_x \rangle$ in IBLs or FSRQs+LBLs is only one times greater than that in HBLs. Finally, in the consideration of the average $\langle \log R_x \rangle$ for total sample is near to 2.0 , we remark that the core X-ray emission within TeV blazars are not prominently dominated by comparison with other two high energy bands (see the discussion below).

The third panel in Figure 1 displays the distribution of the γ -ray core-dominance parameters for three groups. HBLs sample likewise take up a protruding peak in $\log R_\gamma = 1.21$ at a probability density of $\rho = 0.28$. The average value and median is $\langle \log R_\gamma \rangle = 1.82 \pm 1.65$ and 1.31 , separately. The subgroup of IBLs in this case show two peaks. The first one is at $\log R_\gamma = 2.01$ ($\rho = 0.16$) and another at $\log R_\gamma = 5.56$ ($\rho = 0.12$). We find their average is $\langle \log R_\gamma \rangle = 3.63 \pm 2.16$ and the median is 3.17 . Lastly, $\langle \log R_\gamma \rangle = 5.56 \pm 2.37$ and median of 6.18 are reached for FSRQs and LBLs. They peak in $\langle \log R_\gamma \rangle = 6.76$ with $\rho = 0.13$. The distributivity of this parameter is quite similar with $\log R_{\text{radio}}$. Two shapes are nearly the same only differ in the magnitude of $\log R_\gamma$ is enlarging, which indicates (1) the radio emission and γ -ray emission is closely correlative; (2) the γ -ray emission originating within the TeV blazars jets are perhaps stronger beamed than the radio emission. There are nearly half of sources having their core γ -ray luminosity ten thousand times brighter than the extended (or unbeamed) luminosity. However, there are scarcely any sources located in the region of $\log R_{\text{radio}} > 5.0$ and only a small fraction are beyond $\log R_x > 5.0$. Besides, the tendency we obtain here that HBLs \sim IBLs \sim FSRQs+LBLs is consistent with the finding of Pei et al. (2020b) that the γ -ray emission of Fermi-detected FSRQs are more core dominated than are Fermi BL Lacs. The γ -ray producing in BL Lacs is believed to be due to the SSC process, whereas in FSRQs, also including some LBLs, the γ -ray emission is considered to originate from the external-Compton scattering, and to some extent, from the thermal process in the innermost region. Hence one can expect that the γ -ray emission in BL Lacs is mainly from the jet, and in FSRQs it would be from the accretion disk, the broad emission line region, or the dusty torus (e.g., see Prandini & Ghisellini 2022, for a recent review), thus leading to higher $\log R_\gamma$ in BL Lacs

and lower $\log R_\gamma$ in FSRQs, respectively. We reinforce this conclusion in this work that the low-energy TeV-detected blazars commonly show thousands times stronger beaming compared with the high-energy TeV blazars in γ -ray band.

The bottom panel describes the distributions of TeV core-dominance parameters for three groups. The FSRQs+IBLs subclass has $\log R_{\text{TeV}}$ values ranging from 2.6 to 10.51 with an average value of $\langle \log R_{\text{TeV}} \rangle = 6.24 \pm 2.96$. On the other hand, the IBLs subgroup exhibits $\log R_{\text{TeV}}$ values scoping from 21.51 to 9.79 , with an average value of $\langle \log R_{\text{TeV}} \rangle = 4.67 \pm 2.67$. For the HBLs, the $\log R_{\text{TeV}}$ values range from -1.17 to 8.26 with an average value of $\log R_{\text{TeV}}$ are $\langle \log R_{\text{TeV}} \rangle = 2.11 \pm 2.02$. The medians of distributions are 1.61 , 3.62 and 6.31 , separately. These values are over treble larger than that in the radio band and marginally higher than that in the γ -ray emission. The probability density of three subsample peaks in $\log R_{\text{TeV}} = 1.19$ ($\rho = 0.22$) for HBLs, $\log R_{\text{TeV}} = 2.92$ ($\rho = 0.13$) for IBLs, and $\log R_{\text{TeV}} = 5.03$ ($\rho = 0.10$) for LBLs, showing that the range of core dominance of the TeV luminosity is rather drastic. We notice that there two sources in our sample have their TeV core-dominance parameter less than 0 . They are TeV J2359–306 (H 2356-309, $z = 0.165$, $\log R_{\text{TeV}} = -1.17$) and TeV J0847+115 (RBS 0723, $z = 0.198$, $\log R_{\text{TeV}} = -0.19$), and both of them are HBLs. These two sources are found to have also relatively small value of core-dominance parameters in radio, X-ray and γ -ray emission, for example, TeV J2359–306 is listed with $\log R_{\text{radio}} = -0.76$, $\log R_x = -1.07$ and $\log R_{\text{gamma}} = -0.56$. This implies that (i) not all the TeV blazars possess strong beaming effect; (ii) we underestimated the radio core-dominance perhaps since the sources are in low or quiescence state when detected.

Overall, our results suggest that FSRQ+LBL sources tend to exhibit broader distributions of core-dominance parameters, typically occupying higher value ranges. A Kolmogorov–Smirnov test is performed on two subsamples and we find that the null hypothesis (they both are from the same population) cannot be rejected at the confidence level $P = 6.37 \times 10^{-5}$ ($d_{\text{max}} = 0.61$) for FSRQs+LBLs and HBLs+IBLs. Thus, at the 0.0001 level, these two distributions are different. This pattern may indicate that low-energy or low-synchrotron peak blazars generally experience stronger beaming effects across frequency bands. Together, these findings are consistent with the interpretation that multiwavelength emission in our compiled TeV sources is beamed, supporting the potential use of core-dominance parameters in high-energy bands as indicators of beaming effects.

4.2. Correlation between Core-dominance Parameters and Spectral Indices in High Energy Band

Aiming to examine the spectral index decomposition in high energy emission, we cross-checked our sample with other references to seek for the total observed spectral index α_{total}^i in each band. The X-ray indices are taken from Lin & Fan (2018)

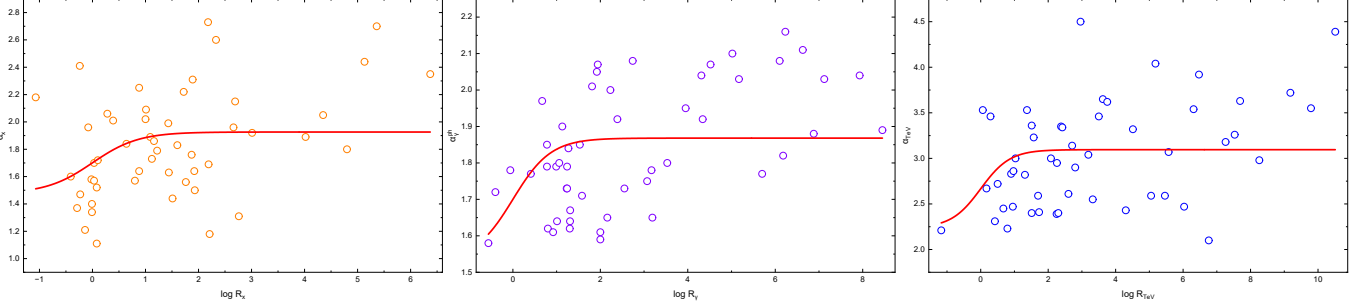


Figure 2. Plot of the correlation that the spectral index against core-dominance parameter in each band.

and Zhou et al. (2024); γ -ray indices are from Zheng et al. (2007), Massaro et al. (2008), and Zhou et al. (2024); and the TeV spectral indices are collected from Gilmore et al. (2012) and Zhong et al. (2018). We are able to fit the correlation using Equation (8), and determine the core index and extended spectral index by minimizing $\Sigma[\alpha_{\text{total}}^i - \alpha_{\text{beamed}}^i R_i / (1 + R_i) + \alpha_{\text{unbeamed}}^i (1 + R_i)]^2$. Results are demonstrated in Figure 2. The panels from left to right hand side are the X-ray index against X-ray core-dominance parameter, γ -ray photon index against γ -ray core-dominance parameter, and TeV spectral index against TeV core-dominance parameter, respectively.

In the X-ray band, the beamed index and unbeamed spectral index can be obtained throughout our whole sample, $\alpha_{\text{beamed}}^X = 1.926 \pm 0.067 / \alpha_{\text{unbeamed}}^X = 1.475 \pm 0.171$. The statistic reduced Chi-square reaches $\chi^2 = 0.139$ and a chance probability $p < 10^{-9}$. The average of observed X-ray spectral indices in references-collected sample is 1.883 ± 0.390 , thus based upon this estimate, we can verdict the total spectral index originates from the core or beamed part in the X-ray emission since the two fitting value of α_{beamed}^X is close to the average one. On the other hand, we find a significant correlation between γ -ray photon index and γ -ray core-dominance parameter (see the middle panel in Figure 2). We derive $\alpha_{\text{beamed}}^\gamma = 1.868 \pm 0.024$ and $\alpha_{\text{unbeamed}}^\gamma = 1.532 \pm 0.127$ with reduced Chi-square $\chi^2 = 0.025$ and a chance probability $p < 10^{-9}$. The collected sample average value of γ -ray photon index is 1.854 ± 0.167 , which is rather near to $\alpha_{\text{beamed}}^\gamma$, indicating the total photon index is mainly attributed to the beamed component in γ -ray band for the TeV blazars. Finally, the fitting core and extended spectral index in TeV emission give $\alpha_{\text{beamed}}^{\text{TeV}} = 3.095 \pm 0.085$ and $\alpha_{\text{unbeamed}}^{\text{TeV}} = 2.238 \pm 0.454$ with $\chi^2 = 0.307$ and a chance probability $p < 10^{-9}$. The average of observed TeV spectral index for the references sample is 3.053 ± 0.507 . This value also approaches to the derived $\alpha_{\text{beamed}}^{\text{TeV}}$, which implies the total TeV emission stems from the beamed or jet component.

Equation (8) suggests that the total spectral index in the high-energy band may be composed of two components, as the high-energy emissions are also strongly beamed, namely the core/beamed and extended/unbeamed parts. By adopting the correlation between the spectral indices and core-dominance

parameters from the radio band to TeV emission, we find that the total observed spectral indices are mainly contributed by the beamed or jet component. This finding supports the two-component emission model in TeV blazars.

4.3. Doppler Factors

We believe the Doppler factors are different at various bands since the emissions from different regions may lead to different Lorentz factors and also the viewing angles between the jet and line-of-sight. Thus the beaming effect on the radiation spectrum is not the same for all bands, and the observed broadband emission originating from blazars is a combination of the beaming effect and intrinsic radiation.

Using the MCMC method and 10,000 sampling, we can constrain the high-energy band Doppler factors within the case of continuous jet and spherical jet. We demonstrate the MCMC result of TeV J0112+227 in Figure 3 (only one source is displayed here. The MCMC results for the whole sample can be found in the supplementary materials). For the continuous jet scenario, we obtain $\Gamma_{\text{TeV}} = 1.39^{+0.65} \Gamma_\gamma$, $\Gamma_\gamma = 1.24^{+0.35} \Gamma_X$, and $\Gamma_X = 1.12^{+0.19}_{-0.09} \Gamma_{\text{radio}}$. The derived Doppler factors are: $\delta_X = 6.48^{+0.57}_{-0.95}$, $\delta_\gamma = 19.87^{+4.12}_{-4.66}$, and $\delta_{\text{TeV}} = 9.88^{+3.89}_{-3.66}$; on the other hand, for the spherical jet model, we also find $\Gamma_{\text{TeV}} = 1.61^{+0.79} \Gamma_\gamma$, $\Gamma_\gamma = 1.30^{+0.53}_{-0.24} \Gamma_X$, and $\Gamma_X = 1.16^{+0.27}_{-0.12} \Gamma_{\text{radio}}$, thus leading to $\delta_X = 6.26^{+0.74}_{-1.19}$, $\delta_\gamma = 18.13^{+5.67}_{-6.03}$, and $\delta_{\text{TeV}} = 7.78^{+4.79}_{-3.99}$ respectively. We listed the derived- δ with upper and lower error in columns (17)–(19) in Table 1.

The distributions of our derived δ_i for the whole sample are shown in Figure 4. The histogram illustrates the statistical distribution of Doppler factors across X-ray, γ -ray and TeV bands, comparing the fits between spherical and continuous geometric models. The propagation upper and lower uncertainties are also labeled. In the X-ray band, the Doppler factor mainly distributed between 1 and 20. The median values are $\delta_X = 3.96$ (continuous) and $\delta_X = 4.03$ (spherical), respectively. In the γ -ray, the δ_γ distribution for the continuous model spans $1 \sim 15$, with medians of $\delta_\gamma = 9.19$ (continuous) and $\delta_\gamma = 9.58$ (spherical). Since the radio Doppler factors on average usually fall in the range of $5 \sim 15$, thus our derived γ -

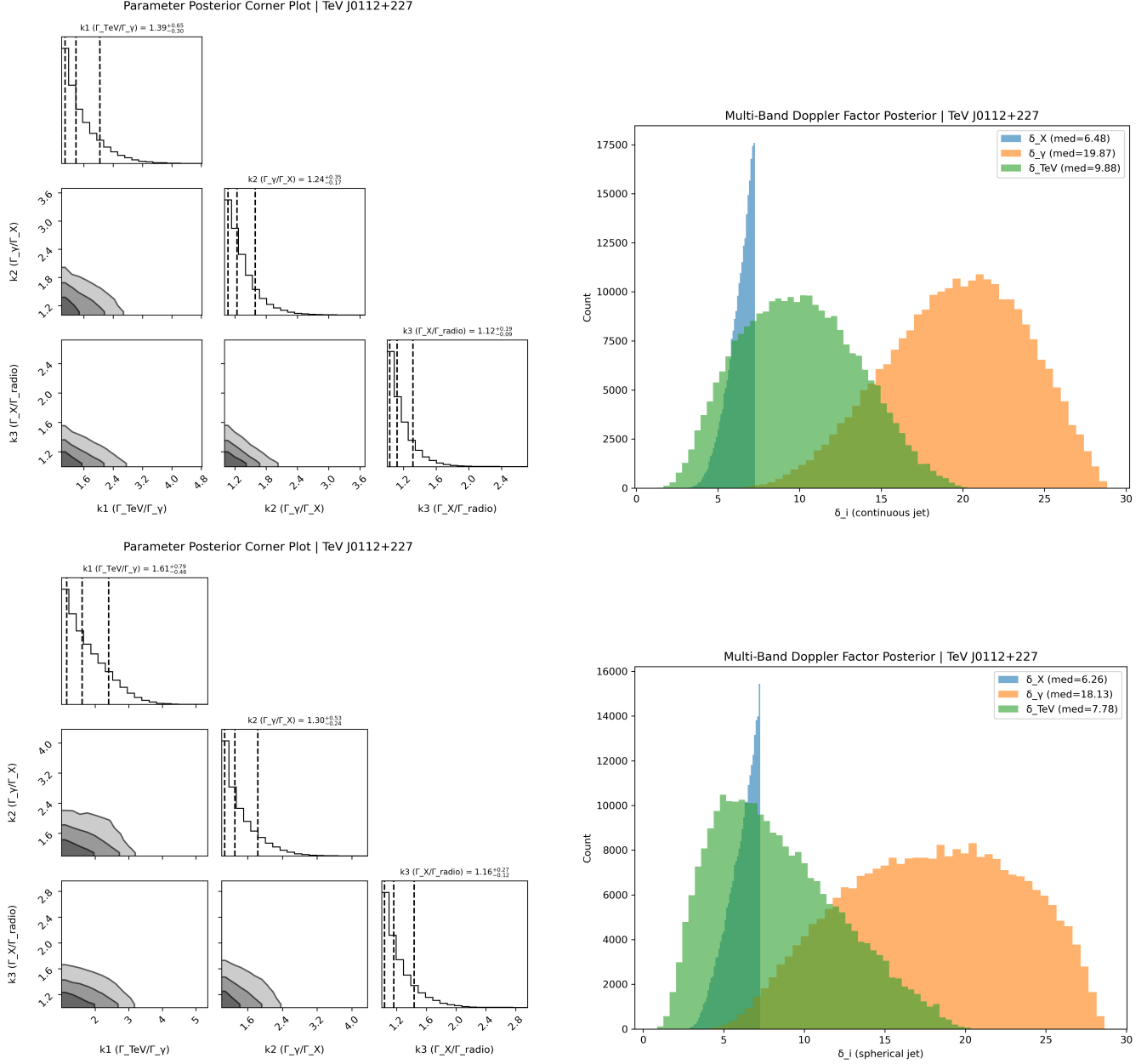


Figure 3. TeV J0112+227: derived results of the Lorentz factors ratio k_1 , k_2 and k_3 via employing the MCMC method; and the Doppler factors we estimate in X-ray, γ -ray and TeV band. The upper row is for the continuous jet model, and the lower row is for spherical case.

ray Doppler factors exhibit similar characteristics with ones in radio band. This can be deemed to another evidence that γ -ray and radio emission is tightly correlative in γ -loud blazars, and also perhaps in TeV blazars. In contrast, TeV Doppler factors are narrowly distributed from 1 to 10, with medians of $\delta_{\text{TeV}} = 4.52$ (continuous) and 4.80 (spherical). These results underscore the energy-dependent nature of Doppler boosting and emphasize the necessity of band-specific radiative and geometric models in blazar studies.

Leveraging the variability timescale and the optical depth property, Pei et al. (2020c) estimated the lower limits on γ -ray Doppler factors for over 800 Fermi-detected blazars,

$$\delta_\gamma \geqslant \left[1.54 \times 10^{-3} (1+z)^{4+2\alpha} \left(\frac{d_L}{\text{Mpc}} \right)^2 \times \left(\frac{\Delta T}{\text{hr}} \right)^{-1} \left(\frac{F_{1 \text{ keV}}}{\mu\text{Jy}} \right) \left(\frac{E_\gamma}{\text{GeV}} \right)^\alpha \right]^{\frac{1}{4+2\alpha}} \quad (18)$$

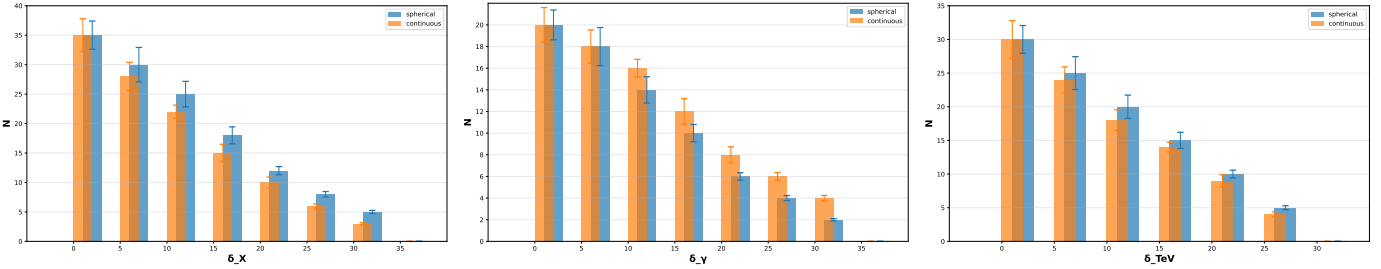


Figure 4. Distributions of estimated Doppler factors in X-ray, γ -ray and TeV band. The red-dashed line and blue-solid line refer to the scenario of spherical and continuous jet respectively, corresponding to $p = 3 + \alpha^i$ and $2 + \alpha^i$, where α^i is the spectral index in X-ray, γ -ray and TeV band.

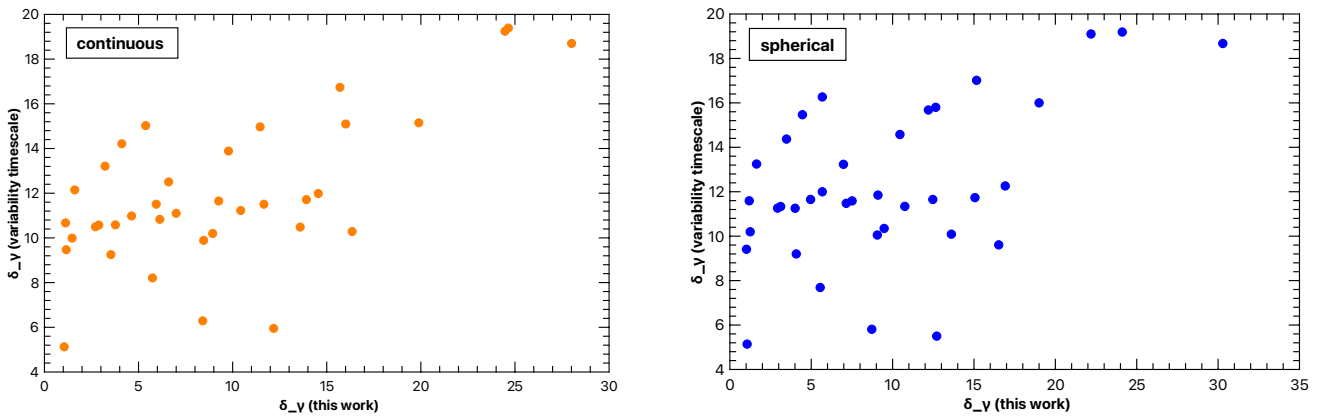


Figure 5. Plot of the γ -ray Doppler factor (δ_γ) estimated from the variability timescale versus the values derived in this work. The left and right panels correspond to the continuous jet and spherical jet scenarios, respectively.

where ΔT is the variability timescale in units of hour, $F_{1\text{ keV}}$ denotes the flux density at 1 keV in units of μJy , E_γ signifies the γ -ray photon energy in units of GeV, α is the X-ray spectral index, and d_L is the luminosity distance in units of Mpc. For comparison, we cross-check this catalog with our current sample and identified 37 common sources. We plot the γ -ray Doppler factors—estimated from the variability timescale—against the results of this work, as shown in Figure 5. Both jet scenarios exhibit a significant correlation: the Pearson correlation coefficient is $r = 0.68$ for the continuous jet and $r = 0.61$ for the spherical jet, with a chance probability of $P < 10^{-4}$ in both cases. This result suggests that the geometry of jet within blazars could be both possibilities in the γ -ray band.

The radio Doppler factors we collected have a median value of $\delta_{\text{radio}} = 10.12 \pm 1.36$. Since these values are not specified to which scenario of jet in their literature, we assume this median is valid for continuous and spherical jet. We find that, for both cases, the Doppler factors decreases with frequency from the radio to X-ray band, while increases from the X-ray to γ -ray band, and in the end, decreases from the γ -ray to TeV band. This variation shows a concave shape from radio to γ -ray emission, and a convex from X-ray to TeV band. Our finding is in line with the discussion in Zeng & Zhang (2011), where

they also discover δ values decrease from radio to X-ray band and increase from the X-ray to γ -ray emission for a sample of γ -loud blazars. Protheroe (2002) also found that the Doppler factors are frequency-dependent with the Doppler factor increasing with frequency in the γ -ray band.

In a leptonic model, for the TeV blazars, the emission from radio to γ -rays is produced from the accelerated electrons with a single distribution mainly via SSC mechanism and the X-ray emission is due to the synchrotron radiation above the synchrotron peak frequency. For a beamed source, the Doppler factor δ_i is nearly equal to the Lorentz factor Γ_i (for a small viewing angle θ_i in the i th high band), resulting in the bulk Lorentz factor a function of the distance to the central black hole. Thus one can expect the Doppler factor will be similar if the emission region for two frequencies are co-spatial, and a farther emission region to the central engine will have a larger Lorentz factor.

Our δ -derived result shows a concave from radio to X-ray while a convex from X-ray to TeV emission, and $\delta_{\text{radio}} \approx \delta_\gamma$ for both $2 + \alpha_i$ or $3 + \alpha_i$, indicating (i) the γ -ray and radio emission are co-spatial within blazar's jet; (ii) the TeV and X-ray emission region are closer to the central black hole. However, the varied δ_i may also be due to the different θ_i in each band, thus our result also reveals that (iii) the diminishing

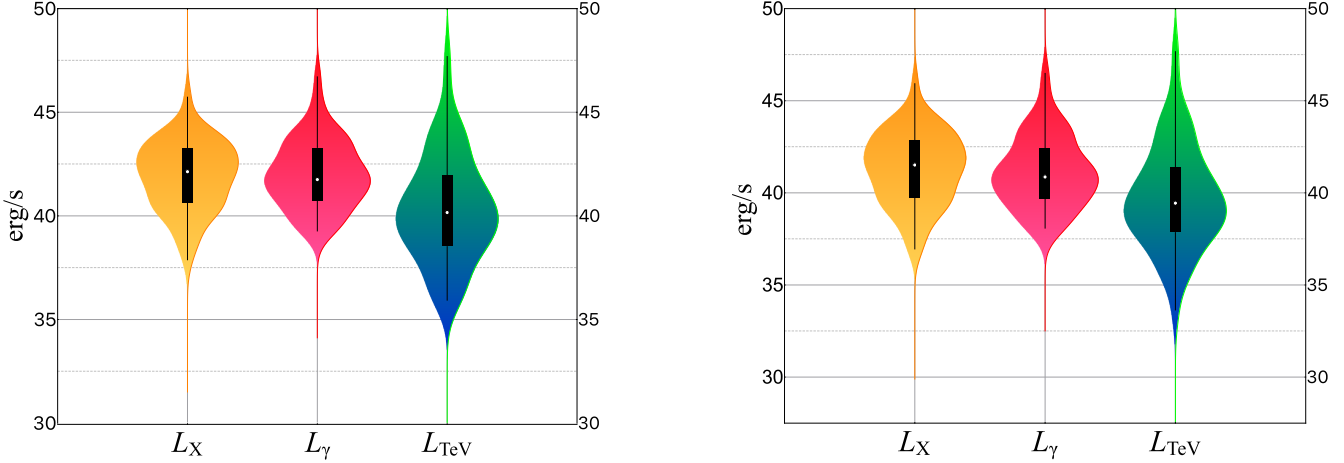


Figure 6. Distributions of de-beamed luminosities in X-ray, γ -ray and TeV band for continuous jet ($2 + \alpha_i$, upper panel) and blob jet ($3 + \alpha_i$, lower panel). The black boxes denote the IQR, i.e., the data range between 25% and 75%, and the central hollow circles are the medians.

tendency from radio to X-ray and γ -ray to TeV band implies the jets change the angles with respect to the line of sight (getting smaller), and the raising tendency from X-ray to γ -ray requires the jets' angles becoming larger. In fact, angle changing from the radio to X-ray bands are observed in some TeV-detected blazars and radio galaxies (e.g., Kataoka et al. 2008; Hogan et al. 2011; Janssen et al. 2021; Marscher et al. 2024).

It is plausible that relativistic particles propagate along radial paths within the jet cone. Although particles at the shock front may experience similar acceleration processes, their directions of motion can differ relative to the observer. Consequently, synchrotron emissions originating from the same shock front may share comparable speeds but could be subject to distinct viewing angles. This geometric arrangement could lead to variations in Doppler factors across different emission frequencies. Furthermore, the spectral index of relativistic particles, denoted as p , may reflect diverse acceleration mechanisms operating within blazar jets, which plays a significant role in estimating Doppler factors. In this work, our results show that δ values tend to be systematically lower for $p = 3 + \alpha_i$ compared to $p = 2 + \alpha_i$ across X-ray, γ -ray, and TeV bands. This pattern could suggest that beaming effects might be more pronounced when accelerated particles are ejected in a continuous jet configuration.

Finally, we need to point out that, for R_i , ground-based IACTs have an inherent flux threshold, which preferentially detects sources with strong beamed core emission (high R_i) since these sources are more likely to exceed the detection limit. This leads to oversampling of high- R_i sources (e.g., FSRQs/LBLs) and underrepresentation of low- R_i sources (e.g., some HBLs like TeV J2359–306 with $\log R_{\text{TeV}} = -1.17$). Additionally, TeV photon absorption by the EBL at higher redshifts means only high- R_i sources (associated with larger δ_i to amplify observed luminosity) are

detectable, further skewing R_i distributions toward higher values. For δ_i , the detection threshold favors sources with larger δ_i because relativistic beaming (enhanced by higher δ_i) amplifies TeV emission, making these sources more detectable. This results in overrepresentation of sources with high bulk Lorentz factors and small viewing angles, as $\delta_i = [\Gamma(1 - \beta \cos \theta)]^{-1}$. For example, sources like PKS 2155–304 with high $\Gamma_{\text{TeV}} \sim 50$ are more easily detected, while low- δ_i sources are missed, leading to an overestimation of median δ_i values (e.g., $\delta_{\text{TeV}} = 12.73$ for continuous jets). These biases may exaggerate observed trends, such as the subclass differences in R_i and the concave-to-convex evolution of δ_i across bands, as the sample does not fully represent the true population of TeV blazars.

4.4. De-beamed Luminosities

The distributions of multiwavelength de-beamed luminosities or intrinsic luminosities are shown in Figure 6, where the upper plot illustrates the continuous jet scenario and the lower one depicts the spherical jet. For the latter case, we obtain that (i) $\log L_X^{\text{in}}$ (erg s^{-1}) are between 37.65 and 45.54 with a median of 41.97. The 1st quartile is $Q_1 = 40.47$ and the 3rd quartile is $Q_3 = 43.06$, showing the data locate in the range of 25%–75%. The interquartile range is IQR = 1.09; (ii) The maximum and minimum of $\log L_\gamma^{\text{in}}$ (erg s^{-1}) is 46.13 and 38.62, respectively, and the median is 41.14. The 1st quartile is $Q_1 = 40.14$ and the 3rd quartile is $Q_3 = 42.70$ (IQR = 1.56); (iii) $\log L_{\text{TeV}}^{\text{in}}$ (erg s^{-1}) is in the range of 35.39–46.75 with a median of 39.58, and $Q_1 = 38.41$ and the 3rd quartile is $Q_3 = 40.97$ (IQR = 2.56). All IQR are labeled using black boxes and the hollow circles stand for the medians in the figure.

For the case of spherical jet, we ascertain: (i) the maximum and minimum of $\log L_X^{\text{in}}$ (erg s^{-1}) is 35.46 and 44.70 with a median of 39.95, $Q_1 = 38.13$ and $Q_3 = 41.43$; (ii)

$\log L_{\gamma}^{\text{in}}$ (erg s^{-1}) is in the scope of 35.54–45.62. The median is 39.60 with $Q_1 = 37.89$ and $Q_3 = 41.25$; (iii) $\log L_{\text{TeV}}^{\text{in}}$ (erg s^{-1}) locates in the range between 31.42 and 45.23, and $Q_1 = 34.93$, $Q_3 = 38.64$, holding a median of 36.57. The IQR are 3.30, 3.36 and 3.71 for X-ray, γ -ray and TeV luminosity, respectively.

Using Equation (17) and corresponding Doppler factors in i th band, we obtain the intrinsic luminosities in high energy emission for our 51 TeV sources. The results reveal that they are still luminous after de-beaming the luminosities. For both two jets scenario, the de-beamed X-ray and γ -ray luminosities display comparable distribution, and the de-beamed TeV luminosities show less bright. One can expect that the de-beamed luminosity is anti-correlated with the Doppler factor in a corresponding band. Yang et al. (2022b) stated $\log L_{\gamma}^{\text{in}} \sim -4.53 \log \delta_{\text{radio}}$ for 255 Fermi-detected blazars at a highly significant confidence level. They also pointed out that there are anti-correlations for the observe luminosities in radio, optical, X-ray and γ -ray band, against the synchrotron peak frequencies, in the first place. However, when the luminosities are de-beamed, those tendencies are changing to the positive correlations, suggesting that the beaming effect is acting an important role in blazar jets.

The bolometric luminosity (L_{bol}) is considered a fundamental physical parameter widely used in blazar studies. Due to the scarcity of simultaneous broadband observational data, several estimators of L_{bol} have been proposed and utilized in practice. For instance, the γ -ray luminosity has been proposed as a potential indicator for bolometric luminosity, following the relation $L_{\text{bol}} \simeq \lambda L_{\gamma}$ (Fossati et al. 1998; Donato et al. 2001; Ghisellini & Tavecchio 2008; Ghirlanda et al. 2010; Xiong & Zhang 2014). However, recent studies have debated the reliability of this approach (e.g., Wang et al. 2017; Tolamatti et al. 2024). Given that γ -ray emission is subject to strong beaming effects, we suggest that the intrinsic γ -ray luminosity might be a more reliable indicator of bolometric luminosity for blazars.

5. Conclusion

In this study, we delve into the beaming effect and physical mechanism governing multiwavelength emission from the TeV-detected blazars. Our approach involved constructing a comprehensive dataset of 51 TeV blazars, encompassing one of key indicators for beaming, namely core-dominance parameters from the radio to TeV band. Utilizing an analytical framework, we successfully implemented a two-component model to unravel the unique TeV emission signatures of these objects. Additionally, we performed a rigorous analysis of the correlations among multiwavelength luminosity, emission core dominance, and spectral index across distinct blazar subclasses. Our salient conclusions are as follows:

1. Our analysis confirms that low-energy peaked TeV blazars exhibit heightened beaming across various frequencies, validating the use of high-energy core-dominance parameters as reliable indicators of beaming effect, as evidenced by the beamed multiwavelength emissions.
2. The predominance of the beamed or jet component in shaping the observed total spectral index in the high-energy band underscores the applicability of the two-component emission model to TeV blazars, which encapsulates both beamed and unbeamed contributions. Our finding points out the total observed emissions are mainly originated from the core or jet component.
3. We estimate the Doppler factors at high-energy bands for both scenarios of continuous and spherical jet launching in TeV blazars. For the case of continuous jet, we obtain median values of $\delta_X = 3.96$, $\delta_{\gamma} = 9.19$ and $\delta_{\text{TeV}} = 4.52$. For spherical blobs, the corresponding values are $\delta_X = 4.03$, $\delta_{\gamma} = 9.58$ and $\delta_{\text{TeV}} = 4.80$. Our results indicate that the beaming effect exhibits significant variation across different wavelength bands. We find a complex energy-dependent trend: the Doppler factor decreases from radio to X-ray, increases from X-ray to γ -ray, and then decreases again from γ -ray to TeV bands. This non-monotonic behavior suggests that emissions at different bands originate from distinct emission regions and/or experience different viewing angles within the jet structure.
4. Using our derived Doppler factors, we can calculate the de-beamed (intrinsic) luminosities in high energy band when the observed luminosities are given.

Acknowledgments

We are deeply grateful to the anonymous referee for the valuable comments and thoughtful suggestions, which greatly improved the quality of our manuscript. Z.Y.P. acknowledges support from the National Science Foundation for Young Scientists of China (grant No. 12103012). Y.J.Q. acknowledges support for the College Student Innovation and Entrepreneurship Training Program of Guangzhou University (No. 202311078059). This work is also partially supported by the National Natural Science Foundation of China (NSFC U2031201, NSFC 11733001, U2031112), Guangdong Major Project of Basic and Applied Basic Research (grant No. 2019B030302001). We also acknowledge the science research grants from the China Manned Space Project with No. CMS-CSST-2021-A06 and the support for Astrophysics Key Subjects of Guangdong Province and Guangzhou City. This research has made use of the NASA/IPAC Extragalactic Database (NED), which is funded by the National Aeronautics and Space Administration and operated by the California Institute of Technology.

ORCID iDs

Zhiyuan Pei <https://orcid.org/0000-0002-4970-3108>

References

- Abdalla, H., Adam, R., Aharonian, F., et al. 2020, *A&A*, **639**, A42
 Abdo, A. A., Ackermann, M., Agudo, I., et al. 2010a, *ApJ*, **716**, 30
 Abdo, A. A., Ackermann, M., Ajello, M., et al. 2010b, *Sci*, **328**, 725
 Abdo, A. A., Ackermann, M., Ajello, M., et al. 2010c, *ApJ*, **715**, 429
 Abdollahi, S., Acero, F., Ackermann, M., et al. 2020, *ApJS*, **247**, 33
 Acciari, V. A., Ansoldi, S., Antonelli, L. A., et al. 2020, *ApJS*, **248**, 29
 Aharonian, F., Akhperjanian, A., Beilicke, M., et al. 2004, *ApJ*, **614**, 897
 Ballet, J., Bruel, P., Burnett, T. H., Lott, B., & The Fermi-LAT collaboration 2023, arXiv:2307.12546
 Begelman, M. C., Blandford, R. D., & Rees, M. J. 1984, *RvMP*, **56**, 255
 Biteau, J., Prandini, E., Costamante, L., et al. 2020, *NatAs*, **4**, 124
 Blandford, R., Meier, D., & Readhead, A. 2019, *ARA&A*, **57**, 467
 Bose, D., Chitnis, V. R., Majumdar, P., & Shukla, A. 2022, *EPJST*, **231**, 27
 Böttcher, M. 2019, *Galax*, **7**, 20
 Cerruti, M. 2020, *Galax*, **8**, 72
 Costamante, L., Ghisellini, G., Giommi, P., et al. 2001, *A&A*, **371**, 512
 Dermer, C. D. 1995, *ApJL*, **446**, L63
 Domínguez, A., Láinez, M., Paliya, V. S., et al. 2024, *MNRAS*, **527**, 4763
 Domínguez, A., Primack, J. R., Rosario, D. J., et al. 2011, *MNRAS*, **410**, 2556
 Donato, D., Ghisellini, G., Tagliaferri, G., & Fossati, G. 2001, *A&A*, **375**, 739
 Fan, J., Yang, J. H., Zhang, J.-Y., et al. 2013, *PASJ*, **65**, 25
 Fan, J. H. 2003, *ApJL*, **585**, L23
 Fan, J. H., Yang, J. H., Liu, Y., et al. 2016, *ApJS*, **226**, 20
 Fan, J.-H., Yang, J.-H., Pan, J., & Hua, T.-X. 2011, *RAA*, **11**, 1413
 Fan, J.-H., Yang, J.-H., Tao, J., Huang, Y., & Liu, Y. 2010, *PASJ*, **62**, 211
 Feain, I. J., Cornwell, T. J., Ekers, R. D., et al. 2011, *ApJ*, **740**, 17
 Finke, J., Ajello, M., Dominguez, A., Desai, A., & Hartmann, D. 2022, *AAS/ High Energy Astrophysics Division*, **19**, 106.47
 Foschini, L., Treves, A., Tavecchio, F., et al. 2008, *A&A*, **484**, L35
 Fossati, G., Maraschi, L., Celotti, A., Comastri, A., & Ghisellini, G. 1998, *MNRAS*, **299**, 433
 Ghirlanda, G., Ghisellini, G., Tavecchio, F., & Foschini, L. 2010, *MNRAS*, **407**, 791
 Ghisellini, G., Padovani, P., Celotti, A., & Maraschi, L. 1993, *ApJ*, **407**, 65
 Ghisellini, G., & Tavecchio, F. 2008, *MNRAS*, **386**, L28
 Ghisellini, G., & Tavecchio, F. 2009, *MNRAS*, **397**, 985
 Gilmore, R. C., Somerville, R. S., Primack, J. R., & Domínguez, A. 2012, *MNRAS*, **422**, 3189
 Hogan, B. S., Lister, M. L., Kharb, P., Marshall, H. L., & Cooper, N. J. 2011, *ApJ*, **730**, 92
 Hovatta, T., Valtaoja, E., Tornikoski, M., & Lähteenmäki, A. 2009, *A&A*, **494**, 527
 Isobe, N., Sato, R., Ueda, Y., et al. 2014, *ApJ*, **798**, 27
 Janssen, M., Falcke, H., Kadler, M., et al. 2021, *NatAs*, **5**, 1017
 Kataoka, J., Stawarz, Ł., Harris, D. E., et al. 2008, *ApJ*, **685**, 839
 Kembhavi, A. 1993, *MNRAS*, **264**, 683
 Konopelko, A., Mastichiadis, A., Kirk, J., de Jager, O. C., & Stecker, F. W. 2003, *ApJ*, **597**, 851
 Liang, J., Zeng, X., Chen, G., et al. 2023, *PASP*, **135**, 084103
 Lin, C., & Fan, J.-H. 2016, *RAA*, **16**, 103
 Lin, C., & Fan, J.-H. 2018, *RAA*, **18**, 120
 Maraschi, L., Fossati, G., Tavecchio, F., et al. 1999, *ApJL*, **526**, L81
 Marscher, A. P. 2016, *Galax*, **4**, 37
 Marscher, A. P., Di Gesu, L., Jorstad, S. G., et al. 2024, *Galax*, **12**, 50
 Massaro, F., Tramacere, A., Cavaliere, A., Perri, M., & Giommi, P. 2008, *A&A*, **478**, 395
 Orr, M. J. L., & Browne, I. W. A. 1982, *MNRAS*, **200**, 1067
 Paiano, S., Treves, A., Franceschini, A., & Falomo, R. 2021, *MNRAS*, **508**, 6128
 Pei, Z., Fan, J., Bastieri, D., Yang, J., & Xiao, H. 2020a, *SCPMA*, **63**, 259511
 Pei, Z., Fan, J., Yang, J., & Bastieri, D. 2020b, *PASP*, **132**, 114102
 Pei, Z., Fan, J., Yang, J., & Bastieri, D. 2020c, *PASA*, **37**, e043
 Pei, Z., Li, Z., Huang, X., et al. 2023, *MNRAS*, **525**, 6214
 Pei, Z.-Y., Fan, J.-H., Bastieri, D., Sawangwit, U., & Yang, J.-H. 2019, *RAA*, **19**, 070
 Pei, Z.-Y., Fan, J.-H., Bastieri, D., et al. 2020d, *RAA*, **20**, 025
 Pei, Z. Y., Fan, J. H., Liu, Y., et al. 2016, *Ap&SS*, **361**, 237
 Planck Collaboration, Ade, P. A. R., Aghanim, N., et al. 2014, *A&A*, **571**, A1
 Prandini, E., & Ghisellini, G. 2022, *Galax*, **10**, 35
 Protheroe, R. J. 2002, *PASA*, **19**, 486
 Punch, M., Akerlof, C. W., Cawley, M. F., et al. 1992, *Natur*, **358**, 477
 Romero, G. E., Cellone, S. A., Combi, J. A., & Andruhow, I. 2002, *A&A*, **390**, 431
 Saldana-Lopez, A., Domínguez, A., Pérez-González, P. G., et al. 2021, *MNRAS*, **507**, 5144
 Shukla, A., Chitnis, V. R., Vishwanath, P. R., et al. 2012, *A&A*, **541**, A140
 Sitarek, J. 2022, *Galax*, **10**, 21
 Stickel, M., Padovani, P., Urry, C. M., Fried, J. W., & Kuehr, H. 1991, *ApJ*, **374**, 431
 Tan, C., Xue, R., Du, L.-M., et al. 2020, *ApJS*, **248**, 27
 Tan, H.-B., Liu, R.-Y., & Böttcher, M. 2024, *MNRAS*, **529**, 903
 Tavecchio, F., Maraschi, L., & Ghisellini, G. 1998, *ApJ*, **509**, 608
 Tolamatti, A., Singh, K. K., & Yadav, K. K. 2024, *Galax*, **12**, 10
 Urry, C. M., & Padovani, P. 1995, *PASP*, **107**, 803
 Urry, C. M., & Shafer, R. A. 1984, *ApJ*, **280**, 569
 Wang, Z., Xue, R., Du, L., et al. 2017, *Ap&SS*, **362**, 191
 Wills, B. J., Wills, D., Breger, M., Antonucci, R. R. J., & Barvainis, R. 1992, *ApJ*, **398**, 454
 Xiao, H., Zhu, J., Fu, L., Zhang, S., & Fan, J. 2022, *PASJ*, **74**, 239
 Xiong, D. R., & Zhang, X. 2014, *MNRAS*, **441**, 3375
 Yang, J., Fan, J., Liu, Y., et al. 2023, *SCPMA*, **66**, 249511
 Yang, J. H., Fan, J. H., Liu, Y., et al. 2022a, *ApJS*, **262**, 18
 Yang, W. X., Wang, H. G., Liu, Y., et al. 2022b, *ApJ*, **925**, 120
 Ye, X.-H., Zeng, X.-T., Huang, D.-Y., et al. 2023, *PASP*, **135**, 014101
 Zeng, H.-D., & Zhang, L. 2011, *RAA*, **11**, 391
 Zeng, X., Zhang, Z., Pei, Z., Xiao, H., & Fan, J. 2022, *Ap&SS*, **367**, 36
 Zhang, Z., Zeng, X., Pei, Z., et al. 2022, *PASP*, **134**, 064101
 Zheng, Y. G., Zhang, X., & Hu, S. M. 2007, *Ap&SS*, **310**, 1
 Zhong, W., Liu, W. G., Zheng, Y. G., et al. 2018, *Ap&SS*, **363**, 179
 Zhou, R. X., Zheng, Y. G., Zhu, K. R., Kang, S. J., & Li, X. P. 2024, *ApJ*, **962**, 22